# Giant Spontaneous Valley Polarization and Adsorption-Induced Topological Phase Transition in Single-Layer 2H-$NbTe_2$

Bo Huang, Shu-Zong Li, Zhixiong Yang, Zhenqing Li, Hongxing Li, and Wei-Bing Zhang*

*Hunan Provincial Key Laboratory of Flexible Electronic Materials Genome Engineering, School of Physics and Electronic Sciences, Changsha University of Science and Technology, Changsha 410114, China*

(Received 10 January 2025; accepted manuscript online 22 April 2025)

Quantum spin Hall state usually emerges in non-magnetic systems, which are typically incompatible with ferromagnetism. Here, we predict that two-dimensional (2D) ferrovalley semiconductor single-layer (SL) 2H-$NbTe_2$ can be transformed into a 2D room-temperature quantum spin Hall insulator through hydrogen (H) atom adsorption. The SL 2H-$NbTe_2$ is found to possess a giant spontaneous valley polarization of 274 meV, which is much larger than those of most available ferrovalley materials. Upon H atom adsorption, a transition from ferromagnetism to non-magnetism emerges. More interestingly, H-adsorbed $NbTe_2$ is predicted to be a quantum spin Hall insulator with a direct band gap of 110 meV (equal to a working temperature of 1267 K). The predicted rich quantum effects render the 2H-$NbTe_2$ a promising candidate for practical valleytronic and topological electronics.

DOI: 10.1088/0256-307X/42/6/067501 CSTR: 32039.14.0256-307X.42.6.067501

Valleytronics have attracted increasing attention in condensed matter physics.[1–6] In two-dimensional (2D) transition metal dichalcogenides (TMDCs), the combined effects of inversion symmetry breaking and strong spin–orbit coupling (SOC) are predicted to generate a pair of energetically degenerate yet unequal valleys.[7–9] Inducing valley polarization in TMDCs is still an essential step for their application in valleytronics. The discovery of ferrovalley materials,[10] which exhibit spontaneous valley polarization, provides new possibilities for the development of valleytronics. These materials, with inversion symmetry breaking and ferromagnetism, are predicted to induce spontaneous valley polarization under the SOC effect. To date, numerous ferrovalley materials[10–15] have been theoretically proposed. However, most candidates exhibit a low valley polarization of less than 100 meV. It is thus necessary to explore more ferrovalley materials with large valley polarization.

On the other hand, quantum spin Hall insulators (QSHIs), which have dissipationless edge states, offer the possibility of low-power electronic devices.[16–23] QSHIs were first theoretically proposed in graphene by Kane and Mele,[24,25] with subsequent experimental confirmation in Hg/CdTe[26,27] and InAs/GaSb[28] quantum wells. Most established QSHIs are non-magnetic, characterized by band inversion and time-reversal-symmetry-protected topological edge states. Consequently, the incompatibility between ferrovalley materials and QSHIs is magnetic state. The key to achieving the transition from the ferrovalley to QSHI states in the same material depends on the modulation of the magnetic properties.

Here, we focus on the TMDCs $NbX_2$ (X = S, Se, Te), which exhibit rich structures (1T, 2H, and 3R) and have been experimentally synthesized.[29–31] Previous theoretical studies[32] identified 2H-$NbX_2$ (X = S, Se) as promising 2D ferrovalley candidates. The heavier Te atom is expected to enhance the SOC effect and valley polarization. Surface adsorption represents an effective strategy for modulating electronic and magnetic properties in 2D materials.[33–36] Notably, adsorption-induced magnetic phase transitions in 2H-$NbSe_2$ have demonstrated the coexistence of ferromagnetism and superconductivity.[35] This precedent suggests that controlled surface adsorption could effectively modulate magnetic states, potentially enabling spontaneous transitions from ferrovalley to QSHI.

In this letter, by first-principles calculations, we predict that single-layer (SL) 2H-$NbTe_2$ is a 2D ferrovalley material with a giant spontaneous valley polarization of 274 meV, arising from the intrinsic ferromagnetism, the inversion symmetry breaking, and strong SOC of the Nb d orbitals. Moreover, hydrogen (H) adsorption on the SL 2H-$NbTe_2$ surface induces a transition from ferromagnetism to non-magnetism. Notably, under the SOC effect, SL H-adsorbed $NbTe_2$ induces a band inversion, transforming into a QSHI with a direct band gap of 110 meV. The topological properties are further confirmed by the calculations of the Wannier charge center (WCC) and edge states. Our work provides a potentially multifunctional material for the design of practical valleytronics and topological electronics.

*Computational Details.* Our density functional theory (DFT) calculations are performed using the Vienna *ab initio* simulation package (VASP)[37,38] within the projector augmented wave method.[39,40] The exchange-correlation

*Corresponding author. Email: zhangwb@csust.edu.cn

© 2025 Chinese Physical Society and IOP Publishing Ltd. All rights, including for text and data mining, AI training, and similar technologies, are reserved.

function is described by the generalized gradient approximation (GGA) of the Perdew–Burke–Ernzerhof (PBE) functional.[41] To account for the strong electronic correlation of Nb d electrons, the GGA+$U$ methods[42] are adopted, in which an effective Hubbard parameter $(U-J)$ of 3 eV, taken from previous work,[32] was used. The plane-wave basis has a kinetic energy cutoff of 500 eV. The 2D Brillouin zone is sampled by a $12\times12\times1$ $k$-point mesh. The structural relaxation is performed until the force on each atom is less than 0.02 eV/Å, with a 20 Å vacuum layer adopted to avoid interlayer interactions. Additionally, the Heyd–Scuseria–Ernzerhof (HSE06) hybrid functional[43] is further performed to obtain a more accurate band gap. The phonon dispersion is calculated with a $4\times4\times1$ supercell via the finite displacement method implemented in the Phonopy code.[44] *Ab initio* molecular dynamics (AIMD) simulations in the canonical ensemble ($6\times6\times1$ supercell, 300 K, 5 ps duration, and 2 fs timestep) verified thermodynamic stability. The maximum localized Wannier functions as implemented in the Wannier90 package[45] and the iterative Green's function method implemented in the WannierTool package[46] are employed to compute the Berry curvature, anomalous Hall conductance, WCC, and edge states.

The SL 2H-$NbTe_2$ possesses an inversion symmetry breaking hexagonal lattice with space group $P\bar{6}m2$ (No. 187), as shown in Figs. 1(a) and 1(b). Each unit cell consists of one Nb atom and two Te atoms, and each Nb atom is surrounded by six Te atoms forming a trigonal prism. The optimized lattice constant of SL $NbTe_2$ is 3.77 Å. To evaluate the stability of SL $NbTe_2$, we also performed the phonon dispersion and molecular dynamics simulation. As shown in Fig. 1(c), the imaginary frequencies are found to be absent in the whole Brillouin zone, indicating that SL $NbTe_2$ is dynamically stable. In addition, room-temperature AIMD results also indicate total potential energies of SL $NbTe_2$ remaining almost invariant during the simulation [Fig. 1(d)], which suggests that SL $NbTe_2$ is thermally stable at 300 K.

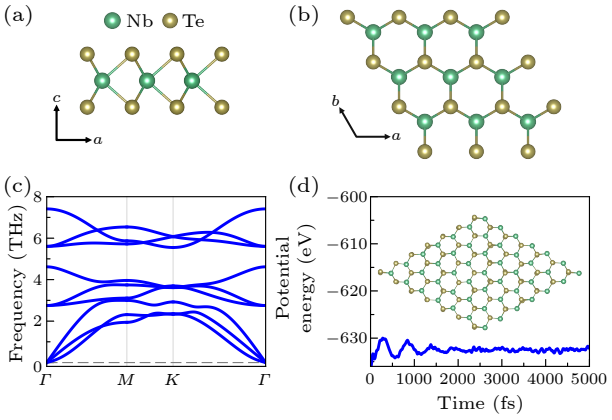


**Fig. 1.** Structure and dynamical stability of SL $NbTe_2$. (a) The side view and (b) the top view of the structure of SL $NbTe_2$. (c) The phonon dispersion of SL $NbTe_2$. (d) Variations of total potential energy of SL $NbTe_2$ during AIMD simulation ($6\times6\times1$ supercell, 5 ps, 300 K). The inset shows the top view of the structure after the AIMD simulations.

According to the crystal field theory, the d orbital in the trigonal environment will split into three groups: $A_1(d_{z^2})$, $E_1(d_{xy},d_{x^2-y^2})$, and $E_2(d_{xz},d_{yz})$. The electron configuration of a $Nb^{4+}$ in SL $NbTe_2$ should be $4d^1$. Clearly, the only one unpaired electron will occupy the lowest-energy $d_{z^2}$ orbital, while the other orbitals are empty. This unique electron configuration will lead to a spin-polarized ground state, and the magnetic moment of each Nb atom is expected to be 1 $\mu_B$.

To explore the magnetic ground state of SL $NbTe_2$, we constructed three magnetic configurations in a $2\times2\times1$ supercell, including ferromagnetic (FM), antiferromagnetic (AFM), and nonmagnetic (NM) states. Our calculations show that the ground state is the FM, which has 260 meV and 467 meV lower energy than those of the AFM and NM states, respectively.

As shown in Fig. 2(a), when magnetism and SOC are not considered, SL $NbTe_2$ is a metal with the Fermi level passing through the state comprising Nb d orbitals. When the spin polarization is considered, degenerate states near the Fermi level are split into spin-up and spin-down states [see Fig. 2(b)]. A FM semiconductor with an indirect band gap of 272 meV appears. In addition, the states of the $K_+/K_-$ valleys are degenerate energetically and also have the same spin component.

As shown in Fig. 2(c), when the SOC is further considered, the indirect band gap becomes 84 meV. The $K_+$ valley of SL $NbTe_2$ up-shifts above the $K_-$ valley in energy, breaking energy degeneracy and inducing spontaneous valley polarization. The valley polarization, defined as the energy difference between the $K_+$ and $K_-$ valleys at the valence band maximum (VBM), is 274 meV, which is larger than most of the available candidates, including $VSe_2$ (78 meV),[10] $VSi_2N_4$ (71 meV),[12] $YI_2$ (108 meV),[47] $LuI_2$ (148 meV),[48] and $FeCl_2$ (101 meV).[49] Notably, Zang *et al.* show that the valley polarization value in

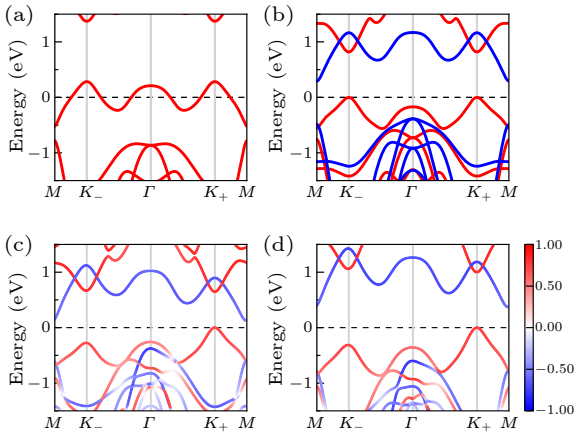


**Fig. 2.** The band structure of SL $NbTe_2$. The band structure calculated using GGA+$U$ methods (a) without the spin polarization and SOC, (b) with spin polarization but without SOC. Red and blue lines represent the spin-up and spin-down bands, and (c) with spin polarization and SOC. The band structure calculated using the HSE06 hybrid functional (d) with spin polarization and SOC. The Fermi level is set at the VBM. The color bar represents the spin contribution of the band, and positive/negative values correspond to opposing spin directions.

$NbSe_2$ ($NbS_2$) is 219 meV (156 meV),[32] which is smaller than the 274 meV in $NbTe_2$. Crucially, valley polarization reverses sign when the magnetization orientation is inverted.

To address the known band gap underestimation of the PBE functional, we performed comparative calculations using the SCAN functional and HSE06 hybrid functional. The calculated results show that the band structures calculated using the SCAN functional and HSE06 hybrid functional [see Fig. 2(d)] are similar to those from GGA+$U$. However, the band gap increases to 634 meV (SCAN) and 370 meV (HSE06), respectively. Notably, the valley polarization increases to 289 meV (SCAN) and 312 meV (HSE06), respectively.

The underlying physics for the large valley polarization in SL $NbTe_2$ arises from the magnetic exchange interaction, inversion symmetry breaking and strong SOC effect. With spin polarization but excluding SOC, the energy between $K_+$ and $K_-$ valleys is degenerate, i.e., $E_\uparrow(K_+) = E_\uparrow(K_-)$, $E_\downarrow(K_+) = E_\downarrow(K_-)$. Notably, the $K_+$ and $K_-$ valleys show large spin splitting (∼1166 meV) near the Fermi level. When including SOC without spin polarization, spin splitting with the same size occurs in the $K_+/K_-$ valley via inversion symmetry breaking. However, the two valleys are energetically degenerate with opposite spin orientations due to time reversal symmetry, i.e., $E_\uparrow(K_+) = E_\downarrow(K_-)$ and $E_\downarrow(K_+) = E_\uparrow(K_-)$. With spin polarization and SOC, the degeneracy of the $K_+/K_-$ valleys is lifted, thereby resulting in spontaneous valley polarization. According to the orbital-resolved band [Fig. S1 in the Supplementary Material (SM)], the large valley polarization in SL 2H-$NbTe_2$ can be explained by the strong SOC effect within Nb $d_{xy}$ and $d_{x^2-y^2}$ orbitals hybridized with Te's p orbital and the magnetic exchange interaction of Nb d electrons. Furthermore, the larger valley polarization in SL 2H-$NbTe_2$, compared to its $NbSe_2/NbS_2$ analogs stems from stronger SOC effects mediated by the heavier Te atoms.

To investigate valley physics in SL $NbTe_2$, we calculated the Berry curvature, which is defined as[50]

$$\Omega(k) = -\sum_n \sum_{n\neq n'} f_n \frac{2\mathrm{Im}\langle\varphi_{nk}|v_x|\varphi_{n'k}\rangle\langle\varphi_{n'k}|v_y|\varphi_{nk}\rangle}{(E_n - E_{n'})^2}, \quad (1)$$

where $f_n$ is the Fermi–Dirac distribution function, $\varphi_{nk}$ is the periodic Bloch wave function with eigenvalue $E_n$, and $v_x$ ($v_y$) is the velocity operator along the $x$ ($y$) direction. The consistency between DFT results and Wannier fitting bands near the Fermi level confirms computational accuracy [Fig. 3(a)]. The calculated Berry curvatures of SL $NbTe_2$ over the Brillouin zone and along high-symmetry lines are shown in Figs. 3(b) and 3(c), respectively. Obviously, the Berry curvatures of the $K_+/K_-$ valleys have opposite signs and unequal absolute values of 120 and −44 $Bohr^2$, respectively.

Due to the large valley polarization in SL $NbTe_2$, the Fermi level can be modulated between $K_+$ and $K_-$ valleys by hole doping. Under an in-plane electric field, Berry curvature works as a pseudo-magnetic field. The charge carrier at the $K_+$ valley possesses an anomalous velocity

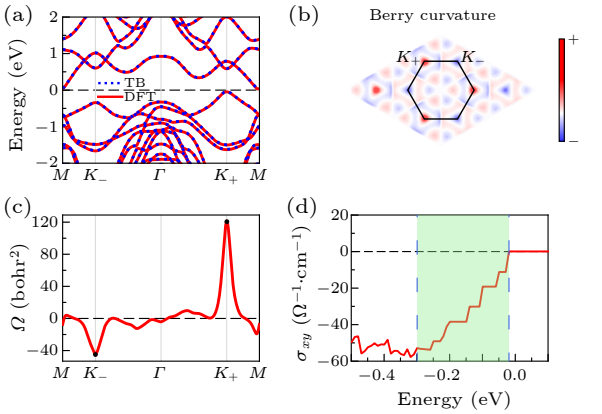


**Fig. 3.** (a) The comparison of band of SL $NbTe_2$ calculated by GGA+$U$ and Wannier fitting methods. (b) The contour map for the Berry curvatures in the Brillouin zone of SL $NbTe_2$. (c) The corresponding Berry curvature along high-symmetry lines. (d) Variation of anomalous Hall conductance with energy.

transverse to the electric field,[51] namely, $\nu \sim E \times \Omega(K_+)$. The spin-down holes at the $K_+$ valley accumulate at the right edge of the sample, leading to the anomalous valley Hall effect. When the direction of magnetization is reversed, the spin-up hole at the $K_-$ valley accumulates on the left edge of the sample. Moreover, by integrating the Berry curvature over the Brillouin zone, the anomalous Hall conductivity reads[52]

$$\sigma_{xy} = \frac{e^2}{\hbar}\int_{\mathrm{BZ}} \frac{\mathrm{d}^2k}{(2\pi)^2} f(k)\Omega(k). \quad (2)$$

As shown in Fig. 3(d), when the Fermi level lies between the valence band energies of the $K_+$ and $K_-$ valleys, as indicated by the two vertical dashed lines, a fully spin- and valley-polarized Hall conductivity emerges. The Hall voltage can be detected with a voltmeter, providing a foundation for valleytronic applications.

Next, we investigate the effects of surface adsorption on SL 2H-$NbTe_2$. As shown in Figs. 4(a) and 4(b), three distinct adsorption sites are considered for the hydrogen atom: $T_{Nb}$ (top position of niobium), $T_{Te}$ (top position of tellurium), and the hollow position. To evaluate site stability, we calculated the adsorption energy ($E_{ad}$), which is defined as

$$E_{ad} = E_{H/NbTe_2} - E_{NbTe_2} - E_H, \quad (3)$$

where $E_{H/NbTe_2}$, $E_{NbTe_2}$, and $E_H$ represent the total energy of the relaxed adsorption system, the clean SL $NbTe_2$, and an isolated H atom, respectively. The calculated adsorption energies are −1.6479 eV ($T_{Nb}$), −1.1862 eV ($T_{Te}$), and −0.6686 eV (H), revealing $T_{Nb}$ as the most stable adsorption site. Consequently, we focus subsequent analysis on the $T_{Nb}$-adsorbed configuration (namely H/$NbTe_2$).

To evaluate the stability of SL H/$NbTe_2$, we have performed phonon dispersion and AIMD simulations. As shown in Fig. 4(c), the imaginary frequency is absent in the whole Brillouin zone, indicating its dynamical stability. Moreover, the total potential energy of SL H/$NbTe_2$ remains almost invariant during the 5 ps AIMD

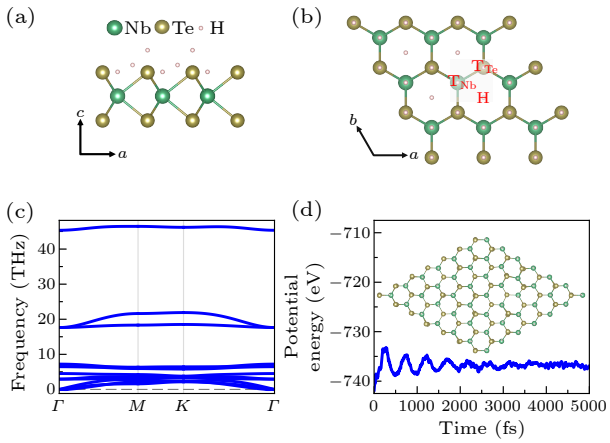


**Fig. 4.** Structural and dynamical stability of SL H/$NbTe_2$. (a) The side view and (b) the top view of the SL H/$NbTe_2$. (c) The phonon dispersion of SL H/$NbTe_2$. (d) Variations of total potential energy of SL H/$NbTe_2$ during AIMD simulation ($6 \times 6 \times 1$ supercell, 5 ps, 300 K). The inset shows the top view structure after the AIMD simulations.

simulation at 300 K, as shown in Fig. 4(d), which suggests that SL H/$NbTe_2$ is thermally stable at 300 K.

Next, we explore the magnetic ground state of SL H/$NbTe_2$. After hydrogen adsorption, the unpaired electrons in SL 2H-$NbTe_2$ form pairs with the electron brought by the H atom, driving a FM-to-NF phase transition. Therefore, we systematically investigated the FM, AFM, and NM states in a $2 \times 2 \times 1$ supercell. The calculations always converge to the NM state regardless of the initial magnetic state. To confirm the magnetic state, we calculated the variation of the energy with the magnetic moment (as shown in Table 1). Our calculations indicate that the energy is lowest at 0 μB, which suggests that the ground state of SL H/$NbTe_2$ is NM. This NM ground state also confirms the above analysis.

**Table 1.** The calculated energy varies with magnetic moment of SL H/$NbTe_2$. The energy of 0 μB is set to 0 meV.

| Magmon monment (μB) | 0 | 1 | 2 | 3 |
|---|---|---|---|---|
| Energy (meV) | 0 | 195 | 842 | 1796 |

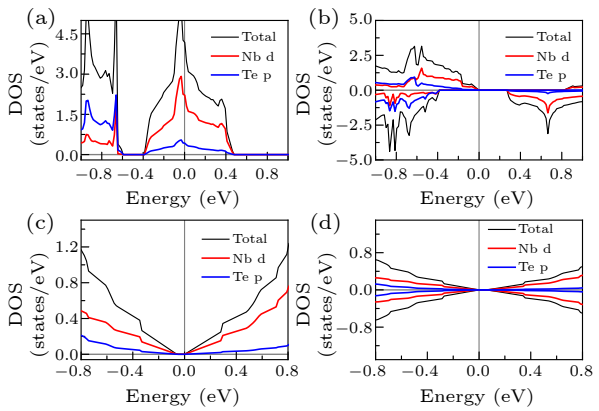


**Fig. 5.** The density of states (DOSs) of SL $NbTe_2$ and SL H/$NbTe_2$. DOS without spin polarization for (a) $NbTe_2$ and (c) SL H/$NbTe_2$, respectively. DOS with spin polarization for (b) SL $NbTe_2$ and (d) SL H/$NbTe_2$, respectively. The Fermi level is set at VBM.

To reveal the FM-to-NM transition mechanism, we calculated the density of states (DOSs) of $NbTe_2$ and H/$NbTe_2$ without and with spin polarization (see Fig. 5). As shown in Fig. 5(a), without spin polarization, the DOS near the Fermi level in $NbTe_2$ is very high, which is mainly contributed by the Nb d orbitals. After considering spin polarization [Fig. 5(b)], these states across the Fermi level in NM states are split into occupied low-energy and unoccupied high-energy states with exchange splitting, which lowers the energy of the system. This electronic instability drives spontaneous spin polarization in SL $NbTe_2$. After the adsorption of hydrogen atoms, a small band gap is formed [as shown in Figs. 5(c) and 5(d)]. This indicates that the NM is stable, which is consistent with the predicted NM ground state of SL H/$NbTe_2$.

Now, we turn our attention to the band structure of SL H/$NbTe_2$. As shown in Figs. 6(a) and 6(b), when SOC is not considered, SL H/$NbTe_2$ is a direct band gap semiconductor with a 53 meV band gap in the $K_+/K_-$ valleys. This is because the absence of magnetism causes the spin-split bands to become degenerate. Meanwhile, the electron brought by the H atom induces an upward shift of the Fermi level, resulting in a transition from a metal to a semiconductor (Fig. S2 in the SM). When SOC is further considered, SL H/$NbTe_2$ remains a direct band gap semiconductor, with the band gap increasing to 110 meV [Figs. 6(c) and 6(d)]. To prove our calculations, we further calculated the band structures with and without SOC using the HSE06 hybrid functional. As shown in Fig. S3 in the SM, SL H/$NbTe_2$ remains semiconducting without SOC, though the band gap decreases to 30 meV. When SOC is considered, the band gap increases to 200 meV. To explore the underlying mechanism of the topological phase transition, we analyze the orbital-resolved band structure of SL H/$NbTe_2$ (Fig. 6). Without SOC, it can be seen that the conduction-band minimum (CBM) is mainly contributed by Nb $d_{xy}$ and $d_{x^2-y^2}$ orbitals, while the VBM is mainly

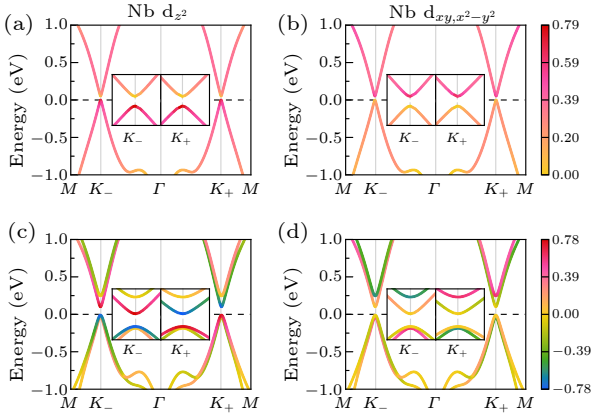


**Fig. 6.** The orbital-resolved band structures of SL H/$NbTe_2$ calculated by GGA+$U$ methods. Without SOC (a) Nb $d_{z^2}$ orbital and (b) Nb $d_{xy}/d_{x^2-y^2}$ orbital, respectively. With SOC (c) Nb $d_{z^2}$ orbital and (d) Nb $d_{xy}/d_{x^2-y^2}$ orbital, respectively. The Fermi level is set at VBM. The insets represent the band structure of $K_+/K_-$ valleys near the Fermi level. The color bar represents the orbital contribution of the band, in which negative (lower limit) and positive (upper limit) represent two opposite spin directions, respectively.

contributed by Nb $d_{z^2}$ orbitals [see Figs. 6(a) and 6(b)]. When SOC is considered, the inversion symmetry breaking lifts the spin degeneracy, inducing spin splitting. Notably, both VBM and CBM are contributed by the Nb $d_{z^2}$ orbitals, suggesting the band inversion between the Nb $d_{z^2}$ and Nb $d_{xy}/d_{x^2-y^2}$ orbitals [see Figs. 6(c) and 6(d)].

As shown above, the SOC leads to a band inversion, which indicates a possible topological phase transition in SL H/$NbTe_2$. To further explore the topological properties of SL H/$NbTe_2$, we calculated the $Z_2$ invariant and edge states. As shown in Fig. 7(a), The evolution of WCC shows an odd number of intersections with any horizontal reference line, confirming that SL H/$NbTe_2$ is a QSHI with $Z_2 = 1$. Moreover, we can also find a one-dimensional edge state connecting the conduction and valence bands in Fig. 7(b). The predicted $Z_2$ number and topologically protected edge state indicate that SL H/$NbTe_2$ is a potential QSHI. As shown above, the calculated topological gap is 110 meV, which corresponds to a working temperature of 1276 K.

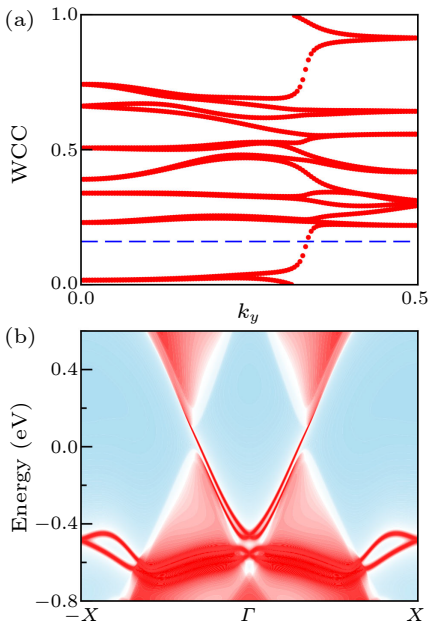


**Fig. 7.** Topological properties of SL H/$NbTe_2$. (a) The evolution of WCC of SL H/$NbTe_2$; (b) the edge states of SL H/$NbTe_2$.

Experimentally, we expect that SL 2H-$NbTe_2$ could be synthesized via a widely used chemical vapor deposition.[53] The valley polarization can be characterized by circularly polarized photoluminescence.[9] Additionally, hydrogen adsorption on SL 2H-$NbTe_2$ can be achieved via hydrogen plasma treatment,[36] while topological edge states are confirmed by scanning tunneling spectroscopy.[54]

In summary, our calculations show that SL $NbTe_2$ is a 2D ferrovalley material with a large spontaneous valley polarization of 274 meV, arising from intrinsic magnetic exchange interactions and a stronger SOC effect. It has opposite but unequal absolute values of Berry curvature at $K_+/K_-$ valleys, driving an anomalous valley Hall effect. Furthermore, hydrogen adsorption induces a transition from a FM to a NM state, thereby transforming the system from ferrovalley materials into QSHIs with a direct band gap of 110 meV. The topological property of SL H/$NbTe_2$ has been confirmed via WCC and edge state calculations. However, it should be noted that achieving precise control over the hydrogen adsorption coverage and site remains challenging. Additionally, structural damage induced by hydrogen adsorption might affect the characterization of edge states and device applications. Nevertheless, our work provides theoretical guidance for designing 2D multifunctional materials for valleytronics and topological electronics.

*Acknowledgments.* This work was supported by the National Natural Science Foundation of China (Grant No. 11874092), the Fok YingTong Education Foundation, China (Grant No. 161005), the Science Fund for Distinguished Young Scholars of Hunan Province (Grant No. 2021JJ10039), the Planned Science and Technology Project of Hunan Province (Grant No. 2017RS3034), and the Postgraduate Scientific Research Innovation Project of Hunan Province (Grant No. CX20240080).

## References

[1] Xu X, Yao W, Xiao D, and Heinz T F 2014 *Nat. Phys.* **10** 343
[2] Zhao J, Liu G B, Chen P, Yao Y, Zhang G, and Du L 2024 *Chin. Phys. Lett.* **41** 066801
[3] Schaibley J R, Yu H, Clark G, Rivera P, Ross J S, Seyler K L, Yao W, and Xu X 2016 *Nat. Rev. Mater.* **1** 16055
[4] Liu Z, Feng W, Xin H, Gao Y, Liu P, Yao Y, Weng H, and Zhao J 2019 *Mater. Horiz.* **6** 781
[5] Deng M, Wang X, Chen J, Li Z, Xue M, Zhou Z, Lin F, Zhu X, and Fang Z 2021 *Adv. Funct. Mater.* **31** 2010234
[6] Zheng J D, Zhao Y F, Tan Y F, Guan Z, Zhong N, Yue F Y, Xiang P H, and Duan C G 2022 *J. Appl. Phys.* **132** 120902
[7] Xiao D, Yao W, and Niu Q 2007 *Phys. Rev. Lett.* **99** 236809
[8] Yao W, Xiao D, and Niu Q 2008 *Phys. Rev. B* **77** 235406
[9] Zeng H, Dai J, Yao W, Xiao D, and Cui X 2012 *Nat. Nanotech.* **7** 490
[10] Tong W Y, Gong S J, Wan X, and Duan C G 2016 *Nat. Commun.* **7** 13612
[11] Zhao P, Ma Y, Lei C, Wang H, Huang B, and Dai Y 2019 *Appl. Phys. Lett.* **115** 261605
[12] Cui Q, Zhu Y, Liang J, Cui P, and Yang H 2021 *Phys. Rev. B* **103** 085421
[13] He Z, Peng R, Feng X, Xu X, Dai Y, Huang B, and Ma Y 2021 *Phys. Rev. B* **104** 075105
[14] Guo S D, Zhu J X, Yin M Y, and Liu B G 2022 *Phys. Rev. B* **105** 104416
[15] Cheng H X, Zhou J, Ji W, Zhang Y N, and Feng Y P 2021 *Phys. Rev. B* **103** 125121
[16] Hasan M Z and Kane C L 2010 *Rev. Mod. Phys.* **82** 3045
[17] Qi X L and Zhang S C 2011 *Rev. Mod. Phys.* **83** 1057
[18] Kou L, Ma Y, Sun Z, Heine T, and Chen C 2017 *J. Phys. Chem. Lett.* **8** 1905
[19] Chen X T, Liu C H, Xu D H, and Chen C Z 2023 *Chin. Phys. Lett.* **40** 097403
[20] Fatemi V, Wu S, Cao Y, Bretheau L, Gibson Q D, Watanabe K, Taniguchi T, Cava R J, and Jarillo-Herrero P 2018 *Science* **362** 926
[21] Zhang F, Kane C L, and Mele E J 2013 *Phys. Rev. Lett.* **111** 056402

[22] Liu X, Lai J, Zhan J, Yu T, Shi W, Liu P, Chen X Q, and Sun Y 2025 *Chin. Phys. Lett.* **42** 037302
[23] Sato M and Ando Y 2017 *Rep. Prog. Phys.* **80** 076501
[24] Kane C L and Mele E J 2005 *Phys. Rev. Lett.* **95** 226801
[25] Kane C L and Mele E J 2005 *Phys. Rev. Lett.* **95** 146802
[26] Bernevig B A, Hughes T L, and Zhang S C 2006 *Science* **314** 1757
[27] König M, Wiedmann S, Brüne C, Roth A, Buhmann H, Molenkamp L W, Qi X L, and Zhang S C 2007 *Science* **318** 766
[28] Knez I, Du R R, and Sullivan G 2012 *Phys. Rev. Lett.* **109** 186603
[29] Zhao S, Hotta T, Koretsune T, Watanabe K, Taniguchi T, Sugawara K, Takahashi T, Shinohara H, and Kitaura R 2016 *2D Mater.* **3** 025027
[30] Xi X, Wang Z, Zhao W, Park J H, Law K T, Berger H, Forró L, Shan J, and Mak K F 2016 *Nat. Phys.* **12** 139
[31] Zhang X, Luo T, Hu X, Guo J, Lin G, Li Y, Liu Y, Li X, Ge J, Xing Y, Zhu Z, Gao P, Sun L, and Wang J 2019 *Chin. Phys. Lett.* **36** 057402
[32] Zang Y, Ma Y, Peng R, Wang H, Huang B, and Dai Y 2021 *Nano Res.* **14** 834
[33] Iyikanat F, Kandemir A, Ozaydin H D, Senger R T, and Sahin H 2017 *Nanotechnology* **28** 495709
[34] Shi H, Pan H, Zhang Y W, and Yakobson B I 2013 *Phys. Rev. B* **88** 205305
[35] Zhu X, Guo Y, Cheng H, Dai J, An X, Zhao J, Tian K, Wei S, Zeng X C, Wu C, and Xie Y 2016 *Nat. Commun.* **7** 11210
[36] Elias D C, Nair R R, Mohiuddin T M G, Morozov S V, Blake P, Halsall M P, Ferrari A C, Boukhvalov D W, Katsnelson M I, Geim A K, and Novoselov K S 2009 *Science* **323** 610
[37] Kresse G and Furthmüller J 1996 *Comp. Mater. Sci.* **6** 15
[38] Kresse G and Furthmüller J 1996 *Phys. Rev. B* **54** 11169
[39] Blöchl P E 1994 *Phys. Rev. B* **50** 17953
[40] Kresse G and Joubert D 1999 *Phys. Rev. B* **59** 1758
[41] Perdew J P, Burke K, and Ernzerhof M 1996 *Phys. Rev. Lett.* **77** 3865
[42] Dudarev S L, Botton G A, Savrasov S Y, Humphreys C J, and Sutton A P 1998 *Phys. Rev. B* **57** 1505
[43] Heyd J, Scuseria G E, and Ernzerhof M 2023 *J. Chem. Phys.* **118** 8207
[44] Togo A, Oba F, and Tanaka I 2008 *Phys. Rev. B* **78** 134106
[45] Pizzi G, Vitale V, Arita R, Blügel S, Freimuth F, Géranton G, Gibertini M, Gresch D, Johnson C, Koretsune T, Ibañez-Azpiroz J, Lee H, Lihm J M, Marchand D, Marrazzo A, Mokrousov Y, Mustafa J I, Nohara Y, Nomura Y, Paulatto L, Poncé S, Ponweiser T, Qiao J, Thöle F, Tsirkin S S, Wierzbowska M, Marzari N, Vanderbilt D, Souza I, Mostofi A A, and Yates J R 2020 *J. Phys.: Condens. Matter* **32** 165902
[46] Wu Q, Zhang S, Song H F, Troyer M, and Soluyanov A A 2018 *Comp. Phys. Commun.* **224** 405
[47] Huang B, Liu W Y, Wu X C, Li S Z, Li H, Yang Z, and Zhang W B 2023 *Phys. Rev. B* **107** 045423
[48] Hu C S, Wu Y J, Liu Y S, Fu S, Cui X N, Wang Y H, and Zhang C W 2023 *Chin. Phys. B* **32** 037306
[49] Zhao P, Dai Y, Wang H, Huang B, and Ma Y 2022 *ChemPhysMater* **1** 56
[50] Thouless D J, Kohmoto M, Nightingale M P, and den Nijs M 1982 *Phys. Rev. Lett.* **49** 405
[51] Xiao D, Chang M C, and Niu Q 2010 *Rev. Mod. Phys.* **82** 1959
[52] Cai T, Yang S A, Li X, Zhang F, Shi J, Yao W, and Niu Q 2013 *Phys. Rev. B* **88** 115140
[53] Xia Y, Chen X, Wei J, Wang S, Chen S, Wu S, Ji M, Sun Z, Xu Z, Bao W, and Zhou P 2023 *Nat. Mater.* **22** 1324
[54] Reis F, Li G, Dudy L, Bauernfeind M, Glass S, Hanke W, Thomale R, Schäfer J, and Claessen R 2017 *Science* **357** 287